Carbon 233 (2025) 119837

Contents lists available at ScienceDirect

Carbon

journal homepage: www.elsevier.com/locate/carbon

# Unveiling high responsivity in on-chip photodetectors with graphene interposed between amorphous and crystalline silicon

T. Crisci [a,b], L. Moretti [c], C. Russo [d], M. Gioffrè [a], M. Iodice [a], G. Coppola [a], M. Casalino [a,*]

[a] Institute of Applied Science and Intelligent Systems "Eduardo Caianiello" - Unit of Naples (ISASI-CNR), Via P. Castellino n. 111, 80131, Naples, Italy
[b] Department of Electrical Engineering and Information Technology, University of Naples Federico II, Via Claudio 21, 80125, Naples, Italy
[c] Department of Mathematics and Physics, University of Campania "Luigi Vanvitelli", Viale Abramo Lincoln, 5, 81100, Caserta, Italy
[d] Institute of Sciences and Technologies for Sustainable Energy and Mobility (STEMS-CNR), P.le V. Tecchio n. 80, 80125, Naples, Italy

A B S T R A C T

In this study, we present an integrated graphene-based photodetector designed for operation around 1550 nm. Our design features a composite waveguide structure consisting of hydrogenated amorphous silicon, graphene, and crystalline silicon. By positioning graphene within this waveguide, we optimize the interaction between the guided mode and the traps at the graphene/amorphous silicon interface. These traps release charge carriers into graphene upon illumination, modulating the thermionic current at the graphene/crystalline silicon Schottky junction. We developed a fabrication protocol compatible with CMOS processes, preserving the integrity of the graphene layer, as confirmed by Raman spectra. The maximum measured responsivity is 1.9 A/W at 1535 nm, corresponding to an external quantum efficiency of 153 %, and a noise equivalent power of 9.6 pW/Hz$^{-1/2}$. The manufacturing process is flexible and does not require sub-micron lithography. Additionally, reducing incident optical power enhances the photodetector responsivity, making it ideal for power monitoring applications in photonic integrated circuits.

## 1. Introduction

Silicon is a known semiconductor widely used in electronic and photonic device applications. However, its inherent characteristics and indirect bandgap size impose limitations on its applicability for photonic devices such as lasers and near-infrared (NIR) photodetectors (PDs) [1].

Recent advancements underscore the potential of graphene (Gr) and Gr-like materials in photonic and optoelectronic applications [2–4]. Particularly noteworthy is the integration of Gr onto Si, which has introduced novel possibilities in NIR photodetection. Concerning waveguide-integrated PDs, four primary detection mechanisms have been predominantly employed: the photovoltaic effect [5], the internal photoemission effect (IPE) [6], the photo-bolometric effect [7,8], and the photo-thermoelectric effect [9].

The photovoltaic effect detection mechanism relies on separating of photoexcited electrons and holes, achievable through an applied electric field generated by energy band bending in metal/Gr/metal structures [10,11]. The IPE approach, on the other hand, involves the use of Gr/Si Schottky junctions and the emission of photoexcited charge carriers from Gr into Si under illumination [6,12–17]. The photo-bolometric effect response is induced by photogenerated hot carriers altering channel resistance, either by changing the carrier concentration or modifying their temperature-dependent mobility [18]. Finally, the photo-thermoelectric effect photocurrent arises from an optically induced temperature gradient and proves particularly efficient in Gr [19–25].

The performance of PDs is often quantified by the responsivity ($R_I$), defined as the ratio of the measured photocurrent ($I_{Ph}$) to the input optical power ($P_{inc}$). On-chip Gr PDs based on photovoltaic effect exhibit a $R_I$ in the range of 0.1–0.36 A/W around 1550 nm [10,11,26] while, in contrast, those based on IPE and photo-bolometric effect demonstrate $R_I$ values of 0.37 A/W [27] and 0.5 A/W [19], respectively. Additionally, integrated waveguide PDs employing photo-thermoelectric effect show $R_I$ values in the range of 0.08–0.36 A/W [19–22]. The photo-thermoelectric effect is particularly suited for PD operation in a voltage mode, allowing direct read-out of the generated photovoltage. In this context, the responsivity can also be expressed as the ratio between the photovoltage ($V_{ph}$) to the input optical power ($R_V = V_{ph}/P_{inc}$), with reported values in the literature ranging from 3.5 to 90 V/W at 1550 nm [22–25]. Lately, integrated photodetectors on silicon-on-insulator (SOI) substrates based on twisted bilayer graphene have demonstrated a responsivity of 0.65 A/W at 1550 nm [28].

A recent significant advancement in vertically illuminated Gr PDs has unveiled and explored a new avenue of research: the utilization of a Gr/crystalline silicon (c-Si) Schottky junction when combined with a layer of hydrogenated amorphous silicon (a-Si:H) to form an a-Si:H/Gr/

* Corresponding author.
*E-mail address:* maurizio.casalino@na.isasi.cnr.it (M. Casalino).

https://doi.org/10.1016/j.carbon.2024.119837
Received 6 September 2024; Received in revised form 12 November 2024; Accepted 17 November 2024
Available online 19 November 2024

c-Si optical microcavity, has yielded remarkable and unexpected results. In this configuration, the experimentally obtained responsivity value reached 26 mA/W, with a Gr/c-Si Schottky barrier of 0.76 eV [29], surpassing the 20 mA/W reported in the literature for IPE-based vertically illuminated Gr/Si PD [30]. The performance improvement has been attributed to a phenomenon that goes beyond IPE, linked to charges trapped at the Gr/a-Si:H interface. The mechanism underlying this effect was comprehensively explained in Ref. [29], where it was first reported. It was observed that under NIR illumination, traps localized at the Gr/a-Si:H interface release charges into the Gr layer. This leads to an upward shift in Gr Fermi level, resulting in a reduction of the Schottky barrier between Gr and c-Si, as evidenced by thermionic current measurements [30]. The impact of depositing an a-Si:H layer on Gr has been explored in the literature, acknowledging that achieving this without negatively affecting the underlying Gr layer is a significant challenge [31]. In their study, Heintze and Zedlitz [32] demonstrated the detrimental impact of ion bombardment on the Gr lattice, evidenced by a sharp increase in defects-related D peak in the Raman spectrum [33]. They also indicated that plasma excitation frequencies above 120 MHz led to lower ion energies, below 25 eV, reducing damage to the Gr lattice.

This work aims to investigate whether the aforementioned effect [29], i.e., the Schottky barrier Photo-modulation ARising from the Key role of traps (referred to as SPARK), can be observed in waveguide PDs based on an a-Si:H/Gr/c-Si guiding structure. Due to the increased light-matter interaction, a further enhancement in responsivity is expected compared to the vertically illuminated counterpart. To this aim, we engineered a hybrid waveguide comprising a-Si:H and c-Si, featuring a single layer Gr (SLG) embedded between these materials. The geometry of the waveguide PD was carefully crafted using numerical simulations employing the finite element method to optimize the overlap of the propagating field intensity on the active Gr strip. Our study highlights that a low-temperature Plasma Enhanced Chemical Vapor Deposition (PECVD) process is adequate for producing high-quality a-Si:H without damaging the Gr lattice, as confirmed by Raman analysis. The deposition of a-Si:H at 100 °C resulted in a refractive index nearly identical to that of c-Si ensuring the preservation of the Gr atomic structure and mitigating potential damage. Responsivity measurements have revealed a correlation with input power, reaching a remarkable value of 1.9 A/W at a low input power $P_{inc} = 400$ pW corresponding to a noise equivalent power (NEP) of 9.6 $pWHz^{-1/2}$, emerging as highly suitable for applications in which low power needs to be detected, such as those related to power monitoring. Despite the inherent scalability of these structures, our study demonstrates that the manufacturing technology is relaxed and inherently flexible, eliminating the need for sub-micron lithography or implantation processes. This outcome carries substantial significance, surpassing the state-of-the-art performance seen in both commercial PDs based on traditional semiconductors (Ge, InGaAs) and Gr PDs utilizing alternative approaches.

## 2. Methods

### 2.1. Device concept

The proposed PD is based on a hybrid waveguide configuration, incorporating a-Si:H, SLG, c-Si components meticulously crafted on a SOI substrate. The design adopts a rib waveguide layout, positioning SLG within the waveguide core, composed of a-Si:H and c-Si, as illustrated in Fig. 1(a). This strategic arrangement enables the concentration of the propagating mode at the SLG/a-Si:H interface, where a substantial number of charges are trapped.

The a-Si:H layer assumes a pivotal role in this photonic structure due to its refractive index closely matching that of c-Si, mitigating the optical density discontinuity encountered by propagating infrared radiation. In Fig. 1(b), we provide a detailed depiction of the active device, emphasizing both the aluminum (Al) electrode and the SLG on c-Si. The SLG/c-Si/Al junction is essentially a metal-semiconductor-metal (MSM) structure, and its corresponding band diagram is presented in Fig. 1(c). This diagram illustrates the scenario where a positive voltage exceeding the flat-band voltage is applied to Al with respect to SLG. Consequently, the

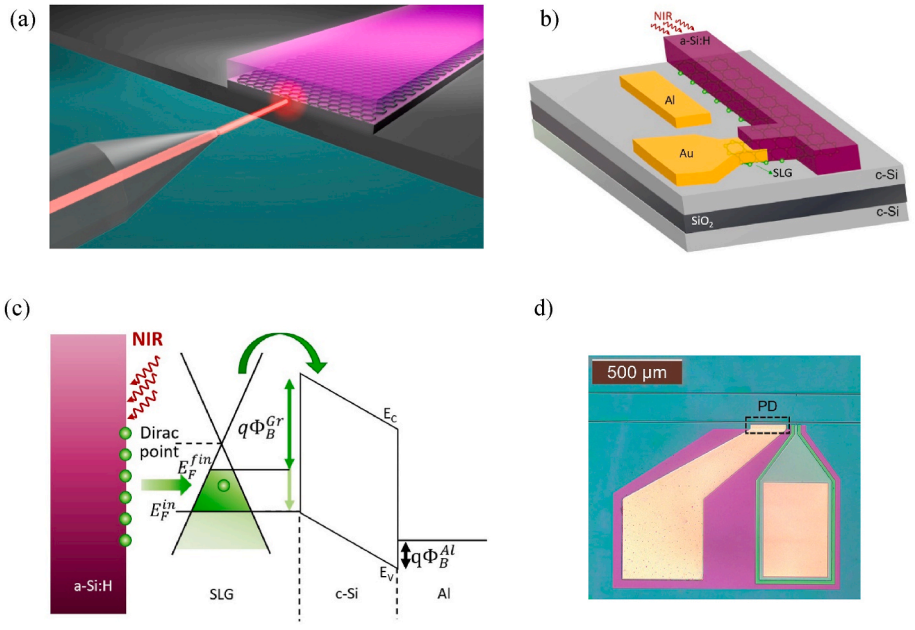


**Fig. 1.** (a) Simplified 3D sketch of the fabricated device when illuminated with a tapered optical fiber. (b) Schematic illustration of the hybrid a-Si:H/SLG/c-Si waveguide. (c) Release of the charges trapped at the a-Si:H/SLG interface under the influence of the light causing a shift of the Fermi energy level from $E_F^{in}$ to $E_F^{fin}$, where $E_F^{in}$ and $E_F^{fin}$ are the initial SLG Fermi energy (in dark conditions) and the final SLG Fermi energy (under illumination) respectively. The Dirac point is the Fermi level of pristine Gr, $q\Phi_B^{Gr}$ is the Schottky barrier height (SBH) at the interface between SLG and c-Si while $q\Phi_B^{Al}$ is the barrier between Al e c-Si. $E_C$ and $E_V$ are the conduction and valence bands of c-Si, which are linearized due to the application of a voltage over the flat band voltage is supposed to be applied. (d) Optical microscope image of the fabricated device.

energy bands are entirely linearized [34].

In Fig. 1(c), we elucidate the detection mechanism [29]: when illuminated at 1550 nm, the charges previously trapped at the interface with a-Si:H are released into the SLG. This injection induces an upward shift in the SLG Fermi level, consequently leading to a reduction in the Schottky SLG/c-Si barrier. This alteration can be observed by measuring the thermionic current.

A comprehensive description of the manufacturing process can be found in Methods, while the optical images illustrating various fabrication steps are provided in Supplementary Materials (Fig. S1). Fig. 1(d) shows an optical microscope image of the finalized device.

### 2.2. Numerical simulations (COMSOL)

To devise an optimized structure, enhancing the interaction between the propagating radiation and the SLG/a-Si:H interface is crucial. We proceed with the assumption that achieving this could involve calculating the minimum length of the SLG required to absorb the propagating modes completely.

This investigation was conducted using the commercial software COMSOL Multiphysics. Specifically, for solving the Maxwell equations numerically, we utilized the "wave optics" module. The numerical simulation was performed in the context of frequency domain analysis, employing a carefully designed two-dimensional model depicting a cross-sectional view of the waveguide. The SLG was modelled as an ultrathin layer with a nominal thickness of 0.335 nm, and scattering boundary conditions were applied to replicate transparent boundaries for scattered waves. In finite element method simulations, detailed meshing is crucial for achieving precise and convergent solutions. For our two-dimensional model, a tailored triangular mesh was employed for each domain, balancing accuracy and computational efficiency. Due to SLG minute thickness, a structured rectangular mesh was used.

Modal analysis was conducted by systematically varying the height of the a-Si:H layer within a range spanning from 70 to 150 nm, incrementing in steps of 5 nm. This step size was chosen considering the resolution inherent in the deposition process (PECVD) used during fabrication. For each specific a-Si:H thickness, the modes supported by the waveguide and the relative extinction coefficients (k) were evaluated. Subsequently, by utilizing the formula $\alpha_P = (4\pi k)/\lambda_0$ (where $\lambda_0$ represents the wavelength in a vacuum), we calculated the absorption coefficient $\alpha_P$ for the propagating mode. To determine the minimum absorption length ($L_{ass}$), we identified the distance at which the intensity of the mode decreases from its initial value ($I_0$) below 1 % in accordance with the Lambert-Beer law $\left(\frac{I(L_{ass})}{I_0} = e^{-\alpha_P L_{ass}} < 1\%\right)$. The analysis focused exclusively on the fundamental mode, which, unlike subsequent modes, exhibits the ability to propagate over longer distances due to its lower extinction coefficient. In this analysis, it is important to note that absorption due to interface defects, which also has an impact, has been neglected. As a result, the calculated length of the graphene strip may be considered an overestimate.

### 2.3. SLG characterization through Raman analysis

SLG characterization via Raman analysis was integral to this investigation, aimed at determining the quality of SLG subsequent to the deposition of a-Si:H. A 532 nm laser served as the excitation source, utilized by an XploRA Raman microscope system (Horiba Jobin Yvon, Kyoto, Japan), employing a 100X objective. Laser power remained below 300 μW, with a 30-s acquisition time and 3 accumulations. Single Lorentzian fitting was employed to extract the positions and intensities of the G and 2D peaks.

### 2.4. SLG and a-Si:H characterization through ellipsometry

For more precise numerical simulations, the complex refractive index of both SLG and a-Si:H was determined via ellipsometry. Spectroscopic ellipsometry data were collected using a phase-modulated spectroscopic ellipsometer (UVSEL, Jobin Yvon Horiba, Palaiseau, France), covering a wavelength range from 300 to 1600 nm. The measurement was conducted at an incidence angle of 70°.

### 2.5. Fabrication

The fabrication process was designed to maintain CMOS compatibility, utilizing techniques with a low thermal budget consistent with the Back-End-of-Line (BEOL) process. In alignment with this objective and to preserve the integrity of the Gr, high-temperature steps were strategically positioned at the initial stage of the process. The main manufacturing steps are depicted in Fig. S1 in Supplementary Materials.

Initiating the process, a standard RCA process ensured thorough cleaning of the SOI substrate. This step was crucial to ensure the absence of contaminants that could introduce defects into the final product. Subsequently, markers necessary for precise alignment in subsequent photolithography steps were defined. After positive resist exposure in photolithography, markers were etched into the c-Si using reactive ion etching (RIE), as illustrated in Fig. S1(a) in Supplementary Materials.

Following this, thermal oxidation was performed, as the elevated temperature (1100 °C) involved could compromise other materials in later steps of PD fabrication, such as the SLG and metals. Under a controlled nitrogen atmosphere, a 4-h process resulted in a 50 nm-thick Silicon Dioxide ($SiO_2$) layer growth. A subsequent photolithography step selectively etched $SiO_2$ using a Buffer Oxide Etch solution (BOE) (Fig. S1 (b) in Supplementary Materials).

The definition of the electrode on c-Si was achieved through a photolithographic process, Al thermal evaporation, and subsequent lift-off. Moreover, a thermal annealing at 475 °C for 30 min was carried out to improve metal adhesion (Fig. S1(c) in Supplementary Materials).

An SLG, purchased from Graphenea Inc. (San Sebastian, Spain), was transferred onto the substrate and then patterned into a 200 μm-long stripe via photolithography and oxygen ($O_2$) plasma dry-etching, as depicted in Fig. S1(d) in Supplementary Materials. Another photolithography step enabled the thermal evaporation of Cr/Au (5/100 nm) for electrical contact with the SLG (Fig. S1(e) in Supplementary Materials). The Cr layer ensured adhesion between Au and the substrate, and a bilayer photoresist system facilitated a gentler lift-off process to avoid SLG damage. The final step involved the definition of the waveguides. An a-Si:H layer, 110 nm-thick, was deposited at 100 °C via PECVD. Then, the waveguides were patterned through photolithography and a studied combination of $CF_4$ and $O_2$ to selectively dry-etch the rib waveguide. Finally, the chip was cleaved, resulting in a 6 mm-long waveguide, as shown in Fig. S1(f) in Supplementary Materials.

### 2.6. Electrical characterization

Electrical characterization of the devices was performed using a probe station along with a Source Meter (Keithley 2410). Two fine metal tips were utilized to establish electrical contact with the device, which was secured on the probe station holder. These tips were positioned on micromanipulators fixed to the optical table via a vacuum pump. By adjusting the voltage across the electrodes, the resulting current through the device was monitored, allowing for investigation into the electrical behavior of the MSM structure and acquisition of I–V characteristics. Each I–V curve represents the average of three measurements.

### 2.7. Optoelectronic characterization

For optoelectronic characterization, the PD was securely positioned on a holder, and electrical contact was established using metal tips. A tunable laser (ANDO AQ4321D) emitted NIR light, operating at telecom wavelengths approximately around 1550 nm. The laser beam was directed onto the waveguide using a tapered optical fiber. To ensure

precise alignment between the tapered fiber and the waveguide facet, an XYZ translation stage managed by the piezoelectric controller Melles Griot MDA 503-75C was employed. The photogenerated current was collected through two metal tips. In measurements conducted with the lock-in technique, an intensity-modulated laser beam was coupled into the waveguide, and the resulting current was sent to a transimpedance amplifier (CVI Melles Griot 13AMP005). This amplifier not only facilitated current collection but also provided bias voltage to the junction. A lock-in amplifier (Signal Recovery 7280 SDP) was used to measure the photogenerated current. The experimental setup is outlined in Fig. S2 in Supplementary Materials. Notably, each measurement represents the average outcome derived from five separate acquisitions.

In measurements conducted without a lock-in amplifier, a continuous-wave (CW) laser beam signal was coupled into the waveguide, and the resulting current was simply measured by a source-meter, as depicted in Fig. S3 in Supplementary Materials. For this purpose, current-voltage (I–V) characteristic curves were systematically measured in dark and illuminated conditions, alternately ten times. Subsequently, the photogenerated current was derived as the difference between the acquired curves under these two distinct conditions.

## 3. Results and discussion

### 3.1. SLG Raman characterization

To ensure the preservation of the SLG, we conducted the deposition of an a-Si:H layer at a relatively moderate process temperature of 100 °C. Subsequently, we employed Raman spectroscopy to assess the impact of this technological procedure on the two-dimensional material. The experimental approach involved transferring SLG onto a glass substrate with a thickness of 100 μm. A controlled deposition of the a-Si:H layer was then performed at 100 °C on half of the SLG area, resulting in the configuration shown in the inset in Fig. 2.

The outcomes of this investigation are depicted in Fig. 2. The Raman spectrum acquired from the SLG capped with a-Si:H retains its characteristic features compared to uncapped SLG: the G peak and the 2D peak remain the two most intense spectral features. Notably, a low-intensity peak corresponding to the D band is observed, indicating an increased presence of defects possibly arising from the plasma treatment. However, these defects are not substantial enough to induce alterations in the atomic structure [35].

Furthermore, a subtle displacement in the positions of the G and 2D peaks is observable. This shift is attributed to the mechanical strain imparted by the presence of the a-Si:H layer, consistent with findings documented in existing literature [36]. A more detailed comparative analysis is provided in Table 1, reporting the mean position, X, and the full width at half maximum, FWHM, of the main peaks fitted using a Lorentzian function. The analysis of the 2D peak shape revealed that the plasma treatment did not significantly alter the single-layer graphene, as indicated by the 2D peak profile. Since the material is single-layer graphene, the observed variation in the 2D/G peak intensity ratio is likely due to changes in the substrate and surrounding environment in which the graphene is placed. This is consistent with known interference effects on the Raman spectrum of graphene on $SiO_2$/Si substrates, as well as the influence of external perturbations on the optical phonon response of graphene [37,38].

### 3.2. Design and numerical simulations

The complexity of the photonic structure has required a finite element approach. To this aim, the numerical simulations were performed with the mode solver COMSOL Multiphysics. While studying the model for implementation, it became imperative to account for constraints stemming from both our manufacturing processes and the available SOI substrates. Even if the device is manufactured starting from a 220 nm-SOI substrate, thermal oxidation is involved in the fabrication process to grow a $SiO_2$ layer of about 50 nm. The thermal oxidation provides for 40 % of Si consumption [28], thus the height of the c-Si layer was fixed at 200 nm in our model. Moreover, the waveguide width, W, is strongly influenced by the resolution of the photolithographic process, therefore, considering our equipment and the geometry of the waveguide, we have set W = 7 μm to have relaxed and repeatable processes. Taking into account these fabrication constraints, the crucial role in the study of the design of the hybrid waveguide has been played by the thickness of the a-Si:H ($t_{a\text{-}Si}$) as shown in Fig. 3(b). The dispersion curves for all relevant materials adopted in the numerical simulations are documented in Supplementary Materials (Fig. S4). These curves have been sourced from literature for $SiO_2$ and c-Si, while for a-Si:H and SLG, they were acquired through ellipsometric measurements

**Table 1**
Raman analysis results.: X denotes the mean position, and FWHM represents the full width at half maximum of the peaks. The subscripts *G* and 2D refer to the two characteristic peaks in the Raman spectrum of graphene.

| | $X_G$ ($cm^{-1}$) | G peak FWHM ($cm^{-1}$) | $X_{2D}$ ($cm^{-1}$) | 2D peak FWHM ($cm^{-1}$) |
|---|---|---|---|---|
| Uncapped SLG | 1586.06 | 13.51 | 2682.19 | 32.33 |
| Capped SLG | 1571.81 | 18.43 | 2666.04 | 21.27 |

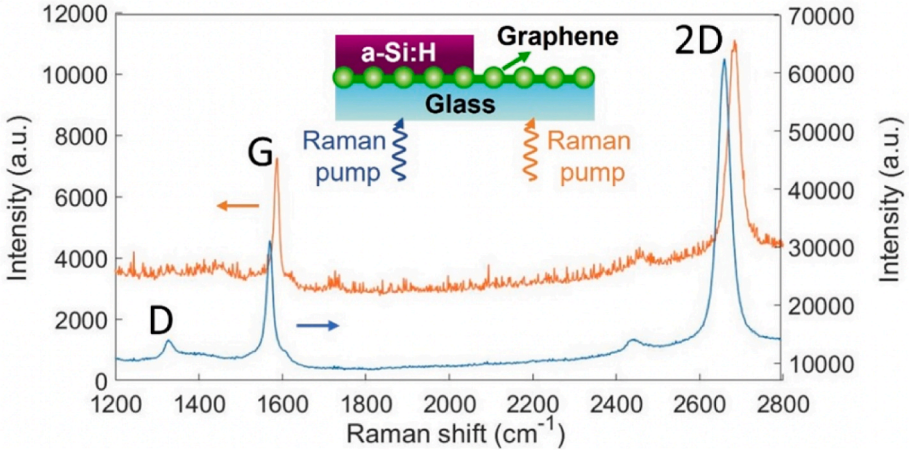


**Fig. 2.** Raman analysis results for both capped and uncapped SLG. In the inset: a sketch of the fabricated sample with one half of the surface containing capped SLG and the other half uncapped SLG. (A colour version of this figure can be viewed online.)

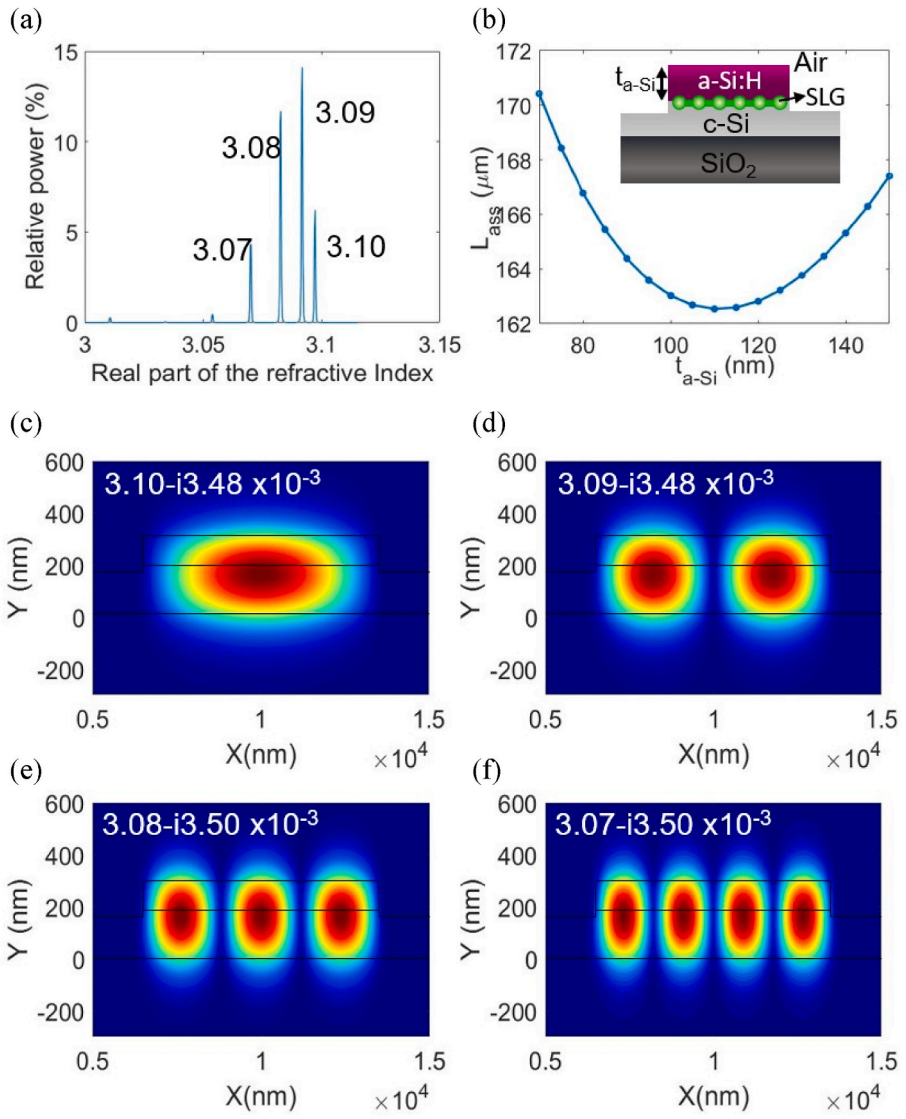


**Fig. 3.** (a) Optical power distribution of the different modes supported by the waveguide. (b) The absorption length $L_{ass}$ necessary for the complete absorption of the propagating fundamental mode in the hybrid waveguide, plotted against $t_{a\text{-}Si}$, and in the inset the sketch of the model implemented in COMSOL. (c)–(f) Electric field distributions of the first 4 modes where the majority of the optical power resides, having complex refractive indexes (c) $3.10 - i3.48 \times 10^{-3}$, (d) $3.09 - i3.48 \times 10^{-3}$, (e) $3.08 - i3.50 \times 10^{-3}$ and (d) $3.07 - i3.50 \times 10^{-3}$. The wase modes are supported by the waveguide utilizing a 110 nm thick a-Si:H layer corresponding to the minimum Lass. (A colour version of this figure can be viewed online.)

performed on the materials produced by our laboratory. To devise an optimized structure, the enhancement of the interaction between the propagating radiation and the SLG/a-Si:H interface is crucial. We have proceeded under the assumption that achieving this could involve calculating the minimum length of the SLG required to absorb the propagating modes completely.

The outcomes of this investigation are presented in Fig. 3. The waveguide has a multimodal behaviour and in Fig. 3(a) the optical power distribution across various modes is depicted. Predominantly, power is concentrated within the first four modes. It is worth noting that the fundamental mode exhibits lower k values, consequently requiring greater length $L_{ass}$ for total absorption. Accordingly, in our analysis, we considered the absorption length of the fundamental mode as a parameter to minimize in order to determine the appropriate thickness $t_{a\text{-}Si}$ of a-Si:H. This study is illustrated in Fig. 3(b). In the inset, the sketch of the implemented model is reported. The minimum length required for nearly complete SLG optical absorption (99 % as detailed in Methods) is 163 μm when the a-Si:H thickness is 110 nm. The electromagnetic field distributions of the first four modes within this waveguide configuration are shown in Fig. 3(c)–(f).

An intriguing comparison arises when examining the minimum length required for an SLG to fully absorb propagating radiation within our embedded structure and comparing it to the length needed for an SLG deposited on top of a conventional SOI rib waveguide. In the latter case, optical absorption results from evanescent field coupling. As demonstrated in Supplementary Materials (Fig. S5), the SLG length in an optimized canonical SOI rib waveguide measures 275.2 μm, surpassing the achievable length in our embedded SLG waveguide.

### 3.3. Photocurrent and responsivity measurements

Our device was initially subjected to electrical investigation, and the I–V curve, obtained using the straightforward setup described in the Methods section, exhibits the expected MSM behavior (Fig. S6 in Supplementary Materials).

The optoelectronic analysis of the PD primarily focuses on its capacity to generate an electrical response upon exposure to incident light, particularly concerning the photogenerated current ($I_{Ph}$) when the PD

active area interacts with NIR radiation. To achieve this, a bias was applied across the junction to capture the photo-excited charge carriers introduced into Si. We employed a lock-in technique, for precise and low-noise $I_{Ph}$ measurements, as described in the Methods section. A tunable laser produced infrared-modulated radiation, and the resulting modulated current, generated in response to the radiation absorbed by the SLG was amplified using a transimpedance amplifier and a lock-in amplifier. Experimental setup is depicted in Fig. S2 in Supplementary Materials. The wavelength of the light ranged from 1520 nm to 1620 nm, with increments of 5 nm. The results, obtained with a −10 V bias applied to the device, are depicted in Fig. 4(a). Within the legend of Fig. 4(a), three different values of incident optical power ($P_{inc}$) are presented, illustrating a direct correlation between higher optical power and increased photogenerated current.

The corresponding spectral responsivity is reported in Fig. 4(b). The incident optical power $P_{inc}$ on the PD, crucial for responsivity calculations, was meticulously measured using a dedicated reference waveguide fabricated specifically for this purpose (Fig. S7). This reference waveguide was strategically positioned in close proximity to the one housing the device, as depicted in Fig. 1(d). Firstly, we quantified the optical power collected at the output of this waveguide ($P_{out1}$) after coupling a known optical power at the input ($P_{inp}$). Then, we repeated the same measurement on the waveguide, now equipped with the PD, resulting in an output power measurement ($P_{out2}$). The difference between $P_{out1}$ and $P_{out2}$ represents the optical power absorbed by the SLG ($P_{ass} = P_{out1}$-$P_{out2}$). Our experimental findings suggest that $P_{out2}$ is negligibly small compared to $P_{out1}$, as expected, owing to the designed length of the SLG strip ensuring 99 % optical absorption of the incident radiation $P_{inc}$. Consequently, nearly all the incident power on the device is absorbed by the Gr strip, making $P_{inc}$ approximately equal to $P_{out1}$. Further details are available in Supplementary Materials.

To conclusively demonstrate that responsivity measurements can be conducted without relying on the lock-in technique, we replicated the experiments using the setup depicted in Fig. S3. This setup employed a CW NIR source and a source-meter. I–V curves were obtained under reverse bias conditions, alternating between dark conditions and exposure to CW optical power of 11.7 nW at 1535 nm, resulting in a responsivity R of 1.1 A/W at −10 V as shown in Fig. 5(a). Fig. 5(b) illustrates the clear separation of photocurrent signals from noise margins. At -10V bias, the photogenerated current measured of 12.6 nA, corresponding to a responsivity of R = 1.1 A/W, is in close agreement with the value obtained via lock-in measurements at 12.8 nW.

### 3.4. Discussion

Remarkably, the PD exhibited a peak responsivity of 1.9 A/W at a wavelength of 1535 nm, with an incident power of approximately 0.4 nW. The corresponding external quantum efficiency is 153 % indicating the presence of a conversion gain that is undoubtedly linked to the presence of traps, as previously highlighted by the photogating effect, and theoretically derived from the SPARK effect in Ref. [29]. As the optical power increases, this value gradually decreases, stabilizing at around 1.1 A/W. Furthermore, Fig. 4(b) illustrates that the responsivity exhibits peaks at various wavelengths and does not display the expected decreasing trend with wavelength, which would be expected if the dominant detection mechanism were IPE. To explore whether the detection mechanism could be attributed to the SPARK effect observed at the a-Si:H/SLG interface, as demonstrated in vertically illuminated devices [29], we conducted a measurement of the PD responsivity as a function of optical power. These measurements were repeated at the wavelength of 1535 nm, where the highest PD response was observed. The experimental results are depicted in Fig. 6.

We observe a decrease in responsivity with increasing incident optical power, mirroring the behavior observed in vertically illuminated devices as reported in Ref. [29]. Consequently, we attempted to fit our experimental data using the equation derived in Ref. [29]:

$$R_I = \frac{I_{Ph}}{P_{inc}} = \frac{A_{Gr} A_N^* T^2 e^{-\frac{q\phi_B^{Gr}}{k_B T}}}{P_{inc}} \left[ e^{\frac{\hbar v_F}{k_B T} \bullet \left( -\sqrt{\pi \left| n_0 - \tau \bullet \eta(P_{inc}) \bullet \frac{P_{inc}}{\hbar\omega \bullet A_{Gr}} \right|} + \sqrt{\pi |n_0|} \right)} - 1 \right] \quad (1)$$

where $A_{Gr}$ is the illuminated active area of the a-Si:H/SLG interface in $cm^2$, $A_N^*$ is the Richardson constant, T is the absolute temperature, $q\Phi_B^{Gr}$ is the SLG/c-Si Schottky barrier, $k_B$ is the Boltzmann constant, $P_{inc}$ is the optical power incident on the active area, ħ is the Planck constant, $v_F$ the Fermi velocity, $n_0$ is the capped SLG doping, $\hbar\omega$ is the photon energy, τ can be physically interpreted as carrier lifetime and η is the conversion efficiency (dimensionless), i.e., the number of charges trapped at the a-Si:H/Gr interface which are released into Gr per incident photon.

During the fitting process the following values were utilized: $A_{Gr} = 1.4 \times 10^{-5}\ cm^2$, $A_N^* = 112\ A/cm^2K^2$, T = 300 K, $k_B = 8.61 \times 10^{-5}$ eV/K, $\hbar = 6.58 \cdot 10^{-16}$ eVs, $v_F = 1.1 \bullet 10^8\ cm/s$ and $\hbar\omega = 0.8\ eV$ while $q\Phi_B^{Gr}$, $\tau \cdot \eta(P_{inc})$ and $n_0$ serve as fitting parameters. Considering that, as demonstrated in Ref. [29], the efficiency-lifetime carrier product can be modelled as a power function $\tau \cdot \eta(P_{inc}) = (\tau \cdot \eta_0)/(P_{inc})^{\beta}$, the results of fitting procedure yield $\tau \cdot \eta_0 = 0.21 \times 10^{-6}\ sW^{\beta}$, β = 0.19, an SLG/c-Si Schottky barrier of $q\Phi_B^{Gr} = 0.56$ eV and $n_0 = 4.2 \times 10^{11}\ cm^{-2}$. The fitting procedure returns an R-square value of 98.3 %, indicating a good agreement between the experimental data and the fitting curve, as depicted in Fig. 6.

It is noteworthy that Fig. 4(b) illustrates a wavelength-dependent behavior of responsivity. This phenomenon arises from the wavelength-dependent ability of the waveguide to confine propagating

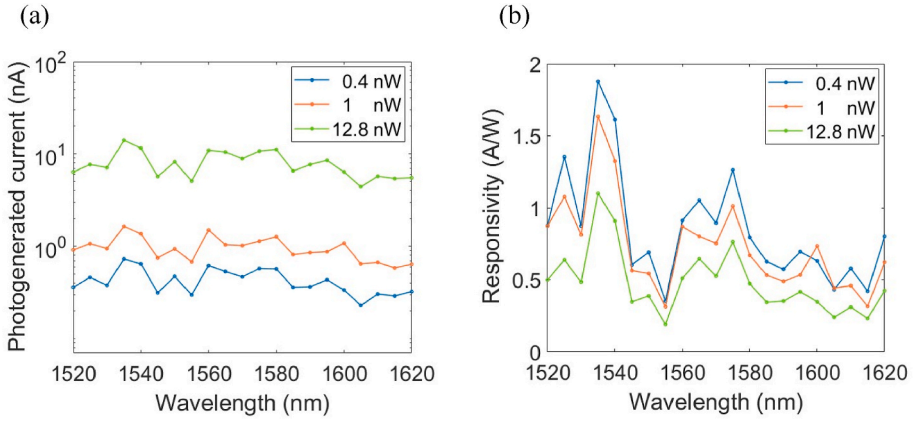


**Fig. 4.** (a) Photogenerated current as a function of the wavelength at various optical power incoming on SLG. (b) Corresponding spectral responsivity. (A colour version of this figure can be viewed online.)

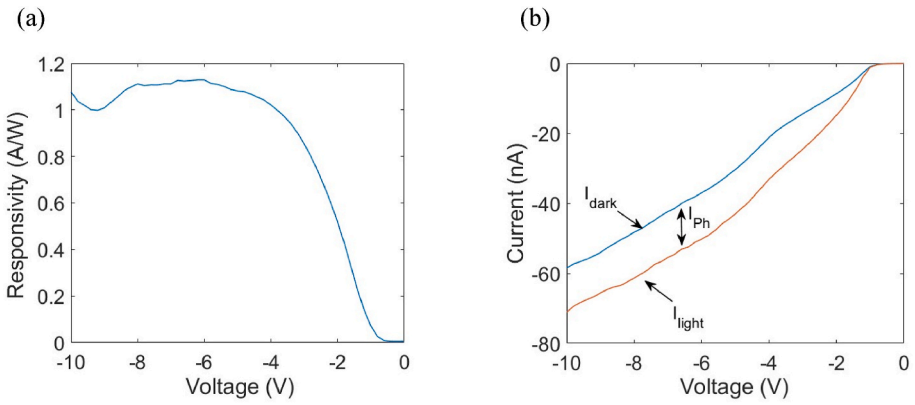


**Fig. 5.** Experimental measurements conducted using a continuous-wave NIR source and a source-meter: (a) Responsivity as a function of voltage, and (b) Reverse I–V curves acquired in dark conditions ($I_{dark}$) and under the NIR signal ($I_{light}$). The difference between $I_{light}$ and $I_{dark}$ represents the photogenerated current ($I_{Ph}$). (A colour version of this figure can be viewed online.)

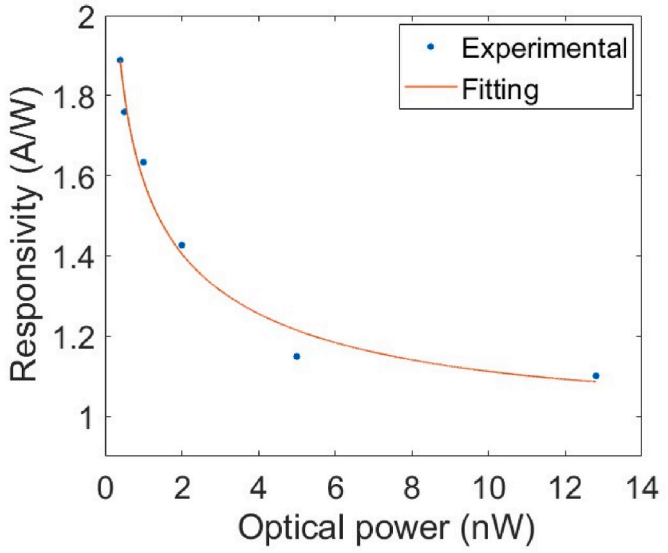


**Fig. 6.** Responsivity of the PD at 1535 nm plotted against incident optical power, along with the corresponding curve fitting based on Eq. (1) from Ref. [29]. (A colour version of this figure can be viewed online.)

radiation, thereby affecting the amount of optical power reaching the PD active region. If this hypothesis holds true, one would expect a peak in responsivity corresponding to the minimum optical power $P_{inc}$. Remarkably, such correspondence has been observed in our experimental measurements and is presented in Fig. S8 in Supplementary Materials. Another crucial factor influencing responsivity is the carrier lifetime τ: while a prolonged carrier lifetime could enhance responsivity, it may also reduce device speed, as seen in graphene PDs that utilize the photogating effect. Carrier lifetime is closely linked to the energy band structure, as well as to defects and impurities, which are significantly influenced by the quality of the a-Si:H and the deposition process parameters. Consequently, meticulous defect engineering is essential to optimize the efficiency-bandwidth product. The Gr-based PD presented in this work, utilizing the SPARK effect, demonstrates higher responsivity values compared to those previously reported in the literature based on the effects investigated up to now, such as photovoltaic effect (0.36 A/W [11]), IPE (0.37 A/W [27]), photo-bolometric effect (0.5 A/W [18]), photo-thermoelectric effect (0.36 A/W [19], and twisted graphene-based PDs (0.65 A/W [28])). As mentioned in the introduction, photo-thermoelectric effect-based PDs operate in voltage mode [22–24], reporting responsivity values in V/W, which complicates comparisons with PDs based on other effects that express responsivity in terms of A/W. Ring resonator structures exploiting the photo-thermoelectric effect have demonstrated record values of 90 V/W at 1550 nm [25]. This value can be easily surpassed by connecting our device to a transimpedance amplifier (TIA) consisting of a feedback resistance of only $R_F = 50\ \Omega$, yielding $R_V = 50\ \Omega \times 1.9$ A/W = 95 V/W (it is worth noting that for comparison purposes, it has been considered useful to exclude the contribution of external bias from the calculation). Under these conditions, it is also straightforward to verify that the device presented in this work exhibits significantly higher sensitivity than that reported in Ref. [25].

The sensitivity can be quantified by considering the NEP, which represents the optical power required, per square root of bandwidth, to generate a photocurrent equal to the noise contribution [39]. NEP can be calculated $NEP = v_n/(R_V\sqrt{B})$ when the responsivity is expressed in V/W, as in Ref. [25], and $NEP = i_n/(R_I\sqrt{B})$ when the responsivity is expressed in A/W, as in the present work, where B denotes the device bandwidth and $v_n$ ($i_n$) represents the noise voltage (current). According to Ref. [25], $v_n = \sqrt{4k_BTBR_D}$ where $R_D$ is the total device resistance, hence an NEP of 38.2 pWHz$^{-1/2}$ can be calculated based on the data reported therein. Conversely, the noise current per square root of bandwidth of our device can be assessed as $\frac{i_n}{\sqrt{B}} = \sqrt{\frac{4k_BT}{R_F} + 2qI_d}$, where considering $R_F = 50\ \Omega$, the dark current $I_d = 60$ nA at −10 V (Fig. 5(b)) and $R_I = 1.9$ A/W, a NEP of only 9.6 pWHz$^{-1/2}$ can be computed. This value is nearly four times lower than what can be derived from Ref. [25].

Our PDs are highly sensitive and therefore particularly suitable for power monitoring applications. Power monitoring within photonic integrated circuits pertains to measuring and testing of optical power levels within the integrated photonic circuit. This process employs integrated photodetectors capable of extracting a minimal amount of optical power circulating at specific points in the circuit to verify the proper functioning of the system. On-chip monitoring and calibration of power levels within photonic integrated circuits may also be crucial for identifying a desired resonance frequency in a sensing circuit or correcting phase discrepancies within an optical phased array (OPA).

## 4. Conclusions

In this study, we extensively investigate the integration of a PD within an a-Si:H/SLG/c-Si waveguide, leveraging the intriguing phenomenon of Schottky barrier photo-modulation, which arises from traps localized at the a-Si:H/SLG interface [29]. Our investigation encompasses thorough numerical simulations aimed at optimizing the positioning of SLG within the waveguide, strategically placing it where the electromagnetic field achieves peak intensity to enhance light-trapped

charge interaction.

Moreover, we meticulously develop a fabrication protocol ensuring compatibility with the back end of the line phase of CMOS processes, thereby preserving SLG integrity. This entails adopting a lower deposition temperature of 100 °C for a-Si:H. Notably, Raman spectra confirm the enduring quality of SLG even when covered by the a-Si:H layer.

Remarkably, our PD demonstrates a maximum responsivity of 1.9 A/W at a wavelength of 1535 nm, corresponding to a NEP of only 9.6 $pWHz^{-1/2}$. To the best of our knowledge, our PD surpasses state-of-the-art achievements in Si-waveguide integrated PDs operating within the third telecom window, outperforming both conventional Si-compatible [40–42] and Gr materials [11,18,19,25,27].

A crucial factor behind this advancement is the manufacturing step involving the deposition of a-Si:H via the PECVD system, which plays a pivotal role in determining device performance. Maintaining graphene integrity is essential, yet this step also provides an opportunity to fine-tune process parameters. By carefully controlling stress, traps, and defects during deposition, significant improvements in efficiency, sensitivity, and speed could be achieved, thus optimizing the overall performance of the device.

Furthermore, despite the inherent scalability of these structures, our study demonstrates the relaxed and inherently flexible nature of manufacturing technology, obviating the need for sub-micron lithography or implantation processes.

Furthermore, it is worth noting that reducing incident optical power can further enhance PD responsivity. Consequently, this heightened performance at low optical power renders the device valuable for power monitoring within photonic integrated silicon circuits, facilitating non-invasive analysis in complex systems where stability and control are paramount.

## CRediT authorship contribution statement

**T. Crisci:** Writing – original draft, Methodology, Investigation, Data curation. **L. Moretti:** Writing – review & editing, Validation, Formal analysis. **C. Russo:** Resources, Methodology, Investigation. **M. Gioffrè:** Resources, Investigation, Data curation. **M. Iodice:** Resources, Investigation. **G. Coppola:** Writing – review & editing, Supervision, Resources. **M. Casalino:** Writing – review & editing, Writing – original draft, Supervision, Project administration, Methodology, Data curation, Conceptualization.

## Disclosures

The authors declare no conflicts of interest.

## Data availability

The datasets generated and analyzed during the current study are available from the corresponding author upon reasonable request.

## Declaration of competing interest

The authors declare that they have no known competing financial interests or personal relationships that could have appeared to influence the work reported in this paper.

## Acknowledgements

We thank M. Medugno for useful discussions and F. Arborino for engaging in discussions on the evaluation of optical power. We extend our gratitude to Vitaliano Tufano and Mauro Feliù from CNR-ISASI Napoli (Italy) for their technical assistance in setting up the system for electro-optical PD characterization.

## Appendix A. Supplementary data

Supplementary data to this article can be found online at https://doi.org/10.1016/j.carbon.2024.119837.

## References

[1] R. Soref, The past, present, and future of silicon photonics, IEEE J. Sel. Top. Quant. Electron. (2006), https://doi.org/10.1109/JSTQE.2006.883151.
[2] Z. Cheng, J. Liao, B. He, F. Zhang, F. Zhang, X. Huang, L. Zhou, One-step fabrication of graphene oxide enhanced magnetic composite gel for highly efficient dye adsorption and catalysis, ACS Sustain. Chem. Eng. 3 (2015) 1677–1685, https://doi.org/10.1021/ACSSUSCHEMENG.5B00383.
[3] Z. Zhang, R. Cai, F. Long, J. Wang, Development and application of tetrabromobisphenol A imprinted electrochemical sensor based on graphene/carbon nanotubes three-dimensional nanocomposites modified carbon electrode, Talanta 134 (2015) 435–442, https://doi.org/10.1016/J.TALANTA.2014.11.040.
[4] I. Rea, M. Casalino, M. Terracciano, L. Sansone, J. Politi, L. De Stefano, Photoluminescence enhancement of graphene oxide emission by infiltration in an aperiodic porous silicon multilayer, Opt Express 24 (2016), https://doi.org/10.1364/oe.24.024413.
[5] T.J. Echtermeyer, P.S. Nene, M. Trushin, R.V. Gorbachev, A.L. Eiden, S. Milana, Z. Sun, J. Schliemann, E. Lidorikis, K.S. Novoselov, A.C. Ferrari, Photothermoelectric and photoelectric contributions to light detection in metal-graphene-metal photodetectors, Nano Lett. 14 (2014) 3733–3742, https://doi.org/10.1021/NL5004762.
[6] M. Casalino, Internal photoemission theory: comments and theoretical limitations on the performance of near-infrared silicon Schottky photodetectors, IEEE J. Quant. Electron. 52 (2016) 4000110, https://doi.org/10.1109/JQE.2016.2532866.
[7] J. Guo, J. Li, C. Liu, Y. Yin, W. Wang, Z. Ni, Z. Fu, H. Yu, Y. Xu, Y. Shi, Y. Ma, S. Gao, L. Tong, D. Dai, High-performance silicon–graphene hybrid plasmonic waveguide photodetectors beyond 1.55 μm, Light Sci. Appl. 9 (2020), https://doi.org/10.1038/s41377-020-0263-6.
[8] X. Du, D.E. Prober, H. Vora, C. Mckitterick, Graphene-based Bolometers, (n.d.).
[9] N.M. Gabor, J.C.W. Song, Q. Ma, N.L. Nair, T. Taychatanapat, K. Watanabe, T. Taniguchi, L.S. Levitov, P. Jarillo-Herrero, Hot carrier-assisted intrinsic photoresponse in graphene, Science 334 (2011) 648–652, https://doi.org/10.1126/SCIENCE.1211384/SUPPL_FILE/GABOR.SOM.PDF.
[10] X. Gan, R.-J. Shiue, Y. Gao, I. Meric, T.F. Heinz, K. Shepard, J. Hone, S. Assefa, D. Englund, Chip-integrated ultrafast graphene photodetector with high responsivity. https://doi.org/10.1038/NPHOTON.2013.253, 2013.
[11] D. Schall, E. Pallecchi, G. Ducournau, V. Avramovic, M. Otto, D. Neumaier, Record high bandwidth integrated graphene photodetectors for communication beyond 180 Gb/s, Opt. Fiber Commun. Conf. (2018), https://doi.org/10.1364/OFC.2018.M2I.4. Pap. M2I.4 Part F84-OFC 2018 (2018) M2I.4.
[12] C. Scales, P. Berini, Thin-film Schottky barrier photodetector models, IEEE J. Quant. Electron. 46 (2010) 633–643, https://doi.org/10.1109/JQE.2010.2046720.
[13] W.-L. Wang, R. Winzenread, B. Nguyen, J.J. Murrin, R.L. Trubiano, High Fill Factor 512 X 512 PtSi Focal Plane Array 1161 (1989) 79–95, https://doi.org/10.1117/12.962691.
[14] U. Levy, M. Grajower, P.A.D. Gonçalves, N.A. Mortensen, J.B. Khurgin, Plasmonic silicon Schottky photodetectors: the physics behind graphene enhanced internal photoemission, APL Photon. 2 (2017) 026103, https://doi.org/10.1063/1.4973537.
[15] M. Casalino, Theoretical investigation of near-infrared fabry–pérot microcavity graphene/silicon Schottky photodetectors based on double silicon on insulator substrates, Micromachines 11 (2020) 708, https://doi.org/10.3390/mi11080708.
[16] M. Casalino, U. Sassi, I. Goykhman, A. Eiden, E. Lidorikis, S. Milana, D. De Fazio, F. Tomarchio, M. Iodice, G. Coppola, A.C. Ferrari, Vertically illuminated, resonant cavity enhanced, graphene-silicon Schottky photodetectors, ACS Nano (2017), https://doi.org/10.1021/acsnano.7b04792.
[17] X. Wang, Z. Cheng, K. Xu, H.K. Tsang, J. Bin Xu, High-responsivity graphene/silicon-heterostructure waveguide photodetectors, Nat. Photonics (2013), https://doi.org/10.1038/nphoton.2013.241.
[18] P. Ma, Y. Salamin, B. Baeuerle, A. Josten, W. Heni, A. Emboras, J. Leuthold, Plasmonically enhanced graphene photodetector featuring 100 Gbit/s data reception, high responsivity, and compact size, ACS Photonics 6 (2019) 154–161, https://doi.org/10.1021/ACSPHOTONICS.8B01234/SUPPL_FILE/PH8B01234_SI_001.PDF.
[19] R.J. Shiue, Y. Gao, Y. Wang, C. Peng, A.D. Robertson, D.K. Efetov, S. Assefa, F.H. L. Koppens, J. Hone, D. Englund, High-responsivity graphene-boron nitride photodetector and autocorrelator in a silicon photonic integrated circuit, Nano Lett. 15 (2015) 7288–7293, https://doi.org/10.1021/ACS.NANOLETT.5B02368/SUPPL_FILE/NL5B02368_SI_001.PDF.
[20] S. Schuler, D. Schall, D. Neumaier, L. Dobusch, O. Bethge, B. Schwarz, M. Krall, T. Mueller, Controlled generation of a p–n junction in a waveguide integrated graphene photodetector. https://doi.org/10.1021/acs.nanolett.6b03374, 2016.
[21] S. Schuler, D. Schall, D. Neumaier, B. Schwarz, K. Watanabe, T. Taniguchi, T. Mueller, Graphene photodetector integrated on a photonic crystal defect waveguide. https://doi.org/10.1021/acsphotonics.8b01128, 2018.
[22] J.E. Muench, A. Ruocco, M.A. Giambra, V. Miseikis, D. Zhang, J. Wang, H.F. Y. Watson, G.C. Park, S. Akhavan, V. Sorianello, M. Midrio, A. Tomadin, C. Coletti,

M. Romagnoli, A.C. Ferrari, I. Goykhman, Waveguide-integrated, plasmonic enhanced graphene photodetectors. https://doi.org/10.1021/acs.nanolett.9b02238, 2019.
[23] V. Miš, S. Marconi, M.A. Giambra, A. Montanaro, L. Martini, F. Fabbri, S. Pezzini, G. Piccinini, S. Forti, T. Terrés, I. Goykhman, L. Hamidouche, P. Legagneux, V. Sorianello, A.C. Ferrari, F.H.L. Koppens, M. Romagnoli, C. Coletti, Ultrafast, zero-bias, graphene photodetectors with polymeric gate dielectric on passive photonic waveguides. https://doi.org/10.1021/acsnano.0c02738, 2020.
[24] S. Marconi, M.A. Giambra, A. Montanaro, V. Mišeikis, S. Soresi, S. Tirelli, P. Galli, F. Buchali, W. Templ, C. Coletti, V. Sorianello, & M. Romagnoli, Photo thermal effect graphene detector featuring 105 Gbit s −1 NRZ and 120 Gbit s −1 PAM4 direct detection, (n.d.). https://doi.org/10.1038/s41467-021-21137-z.
[25] S. Schuler, J.E. Muench, A. Ruocco, O. Balci, D. van Thourhout, V. Sorianello, M. Romagnoli, K. Watanabe, T. Taniguchi, I. Goykhman, A.C. Ferrari, T. Mueller, High-responsivity graphene photodetectors integrated on silicon microring resonators, (n.d.). https://doi.org/10.1038/s41467-021-23436-x.
[26] Y. Ding, Z. Cheng, X. Zhu, K. Yvind, J. Dong, M. Galili, H. Hu, N.A. Mortensen, S. Xiao, L.K. Oxenløwe, Ultra-compact integrated graphene plasmonic photodetector with bandwidth above 110 GHz, Nanophotonics 9 (2020) 317–325, https://doi.org/10.1515/NANOPH-2019-0167/DOWNLOADASSET/SUPPL/NANOPH-2019-0167_SUPPL.ZIP.
[27] I. Goykhman, U. Sassi, B. Desiatov, N. Mazurski, S. Milana, D. De Fazio, A. Eiden, J. Khurgin, J. Shappir, U. Levy, A.C. Ferrari, On-chip integrated, silicon-graphene plasmonic Schottky photodetector with high responsivity and avalanche photogain, Nano Lett. (2016), https://doi.org/10.1021/acs.nanolett.5b05216.
[28] Q. Wu, J. Qian, Y. Wang, L. Xing, Z. Wei, X. Gao, Y. Li, Z. Liu, H. Liu, H. Shu, J. Yin, X. Wang, H. Peng, Waveguide-integrated twisted bilayer graphene photodetectors, Nat. Commun. 15 (2024), https://doi.org/10.1038/s41467-024-47925-x.
[29] T. Crisci, P. Maccagnani, L. Moretti, C. Summonte, M. Gioffrè, R. Rizzoli, M. Casalino, The physics behind the modulation of thermionic current in photodetectors based on graphene embedded between amorphous and crystalline silicon, Nanomaterials 13 (2023) 872, https://doi.org/10.3390/NANO13050872/S1.
[30] S.M. Sze, K.K. Ng, Physics of semiconductor devices. Simon M. Sze, Kwok K. Ng, Phys. Semicond. Devices, third ed., John Wiley Sons, Inc., NJ, 2007, 3rd Ed.
[31] M. Müller, M. Bouša, Z. Nka Hájková, M. Ledinský, A. Fejfar, K. Drogowska-Horná, M. Kalbáč, O. Frank, J. Heyrovský, Transferless Inverted Graphene/Silicon Heterostructures Prepared by Plasma-Enhanced Chemical Vapor Deposition of Amorphous Silicon on CVD Graphene, (n.d.). https://doi.org/10.3390/nano10030589.
[32] M. Heintze, R. Zedlitz, New diagnostic aspects of high rate a-Si:H deposition in a VHF plasma, J. Non-Cryst. Solids 198–200 (1996) 1038–1041, https://doi.org/10.1016/0022-3093(96)00035-X.
[33] P. Ahlberg, F.O.L. Johansson, Z.-B. Zhang, U. Jansson, S.-L. Zhang, A. Lindblad, T. Nyberg, Defect formation in graphene during low-energy ion bombardment, Apl. Mater. 4 (2016) 046104, https://doi.org/10.1063/1.4945587.
[34] S.M. Sze, D.J. Coleman, A. Loya, Current transport in metal-semiconductor-metal (MSM) structures, Solid State Electron. 14 (1971) 1209–1218, https://doi.org/10.1016/0038-1101(71)90109-2.
[35] L. Malard, M. Pimenta, G. Dresselhaus, M. Dresselhaus, Raman spectroscopy in graphene, Phys. Rep. 473 (2009) 51–87, https://doi.org/10.1016/j.physrep.2009.02.003.
[36] N. Ferralis, Probing mechanical properties of graphene with Raman spectroscopy, (n.d.). https://doi.org/10.1007/s10853-010-4673-3.
[37] D. Yoon, H. Moon, Y.W. Son, J.S. Choi, B.H. Park, Y.H. Cha, Y.D. Kim, H. Cheong, Interference effect on Raman spectrum of graphene on SiO2/Si, Phys. Rev. B - Condens. Matter Mater. Phys. 80 (2009) 1–6, https://doi.org/10.1103/PhysRevB.80.125422.
[38] N. Bendiab, J. Renard, C. Schwarz, A. Reserbat-Plantey, L. Djevahirdjian, V. Bouchiat, J. Coraux, L. Marty, Unravelling external perturbation effects on the optical phonon response of graphene, J. Raman Spectrosc. 49 (2018) 130–145, https://doi.org/10.1002/jrs.5267.
[39] Safa O Kasap, Optoelectronics and Photonics, 2013.
[40] S. Assefa, F. Xia, Y.A. Vlasov, Reinventing germanium avalanche photodetector for nanophotonic on-chip optical interconnects. https://doi.org/10.1038/nature08813, 2010.
[41] D. Benedikovic, L. Virot, G. Aubin, J.M. Hartmann, F. Amar, X. Le Roux, C. Alonso-Ramos, É. Cassan, D. Marris-Morini, J.M. Fédéli, F. Boeuf, B. Szelag, L. Vivien, Silicon-germanium receivers for short-wave-infrared optoelectronics and communications High-speed silicon-germanium receivers (invited review), Nanophotonics 10 (2021) 1059–1079, https://doi.org/10.1515/NANOPH-2020-0547/ASSET/GRAPHIC/J_NANOPH-2020-0547_FIG_002.JPG.
[42] S. Lischke, A. Peczek, J.S. Morgan, K. Sun, D. Steckler, Y. Yamamoto, F. Korndamp, C. Mai, S. Marschmeyer, M. Fraschke, A. Kramp, A. Beling, L. Zimmermann, Ultra-fast germanium photodiode with 3-dB bandwidth of 265 GHz, (n.d.). https://doi.org/10.1038/s41566-021-00893-w.